JACS
JOURNAL OF THE AMERICAN CHEMICAL SOCIETY
COMMUNICATION
pubs.acs.org/JACS

Spectral Diffusion at the Water/Lipid Interface Revealed by Two-Dimensional Fourth-Order Optical Spectroscopy: A Classical Simulation Study

Yuki Nagata* and Shaul Mukamel

Department of Chemistry, University of California, Irvine, California 92697, United States

Ⓢ *Supporting Information*

ABSTRACT: Using a classical simulation protocol for nonlinear optical signals, we predict the two-dimensional (2D) spectra of water near a monolayer of [1,2-dimytristoyl-*sn*-glycero-3-phosphatidylcholine] (DMPC) generated by three IR probe pulses followed by one visible probe pulse. Sum-frequency-generation 1D spectra show two peaks of the OH stretch representing two environments: near-bulk water nonadjacent to DMPC and top-layer water adjacent to DMPC. These peaks create a 2D pattern in the fourth-order signal. The asymmetric cross-peak pattern with respect to the diagonal line is a signature of coherence transfer from the higher- to the lower-frequency modes. The nodal lines in the imaginary part of the 2D spectrum show that the near-bulk water has fast spectral diffusion resembling that of bulk water despite the orientation by the strong electrostatic field of DMPC. The top-layer water has slower spectral diffusion.

Interfacial water plays an essential role in the stabilization and functionality of membranes and proteins attached to membranes. Since the cell membrane of living organisms consists primarily of phospholipid bilayers, the water/phospholipid monolayer interface is a good model system for studying water−membrane interactions. A layer of water with a thickness of ~10 Å is oriented by the strong electrostatic interactions with the lipid.[1] Vibrational spectra of interfacial water are distinct from those of bulk water. A single ~3400 cm^{-1} OH stretch in the IR spectrum of bulk water is split into two peaks at 3100−3300 cm^{-1} (L, lower) and 3300−3500 cm^{-1} (H, higher) in the second-order sum-frequency-generation (SFG) spectrum.[2] Time-resolved SFG experiments have revealed that the dynamics is different as well: the H peak exhibits a longer relaxation time (~600 fs) than the bulk (~200 fs).[3] Our recent molecular dynamics (MD) simulation of the SFG spectra at the water/[1,2-dimytristoyl-*sn*-glycero-3-phosphatidylcholine] (DMPC) interface showed that the L and H peaks originate from the OH stretches of near-bulk water nonadjacent to DMPC and the top-layer water adjacent to DMPC, respectively.[4] An important open issue is how rapidly the configurations of the interfacial water vary. A good experimentally accessible indicator for ultrafast configuration changes is provided by the fluctuations of frequencies (spectral diffusion). Spectral diffusion probes the surrounding molecular structures and local dynamics of water at lipid and biological interfaces. Even though both the top-layer and near-bulk water are oriented to the DMPC layer by the strong electrostatic interactions with the hydrophilic part of DMPC, it is not clear what is the timescale of the configurational rearrangement.

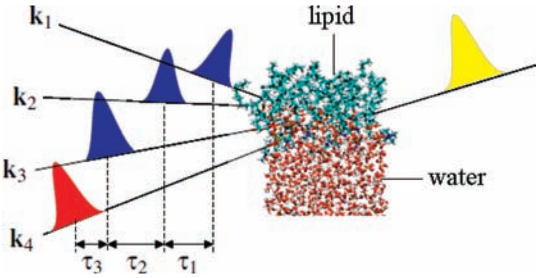

Figure 1. The fourth-order IR−IR−IR−vis experiment. The blue, red, and yellow pulses represent the IR, visible, and detection pulses; $\mathbf{k}_1$, $\mathbf{k}_2$, $\mathbf{k}_3$, and $\mathbf{k}_4$ are the wavevectors of the probe pulses, and τ_1, τ_2, and τ_3 represent the delays between the probe pulses.

The heterogeneity of water configuration near DMPC has been examined by two-color pump−probe IR and two-dimensional (2D) IR experiments in low-hydrated DMPC[5] and DNA;[6] water attached to DMPC was found to be more heterogeneous than bulk water. Since low-hydrated DMPC contains no bulk water, the top-layer water adjacent to DMPC is dominant and the near-bulk water connecting the top-layer water with the bulk is not observed.[5] At higher levels of hydration, the interfacial contribution is masked by the bulk contribution in odd-order optical signals. Thus, probing spectral diffusion of interfacial water requires even-order interface-specific 2D techniques where the bulk contribution is eliminated by symmetry. Second-order 2D IR−IR surface-specific spectroscopy, which has two time delays analogous to 2D Raman spectroscopy,[7] has been proposed.[8,9] An alternative 2D surface-specific spectroscopy uses the fourth-order IR−IR−IR−vis (IIIV)[10] pulse configuration shown schematically in Figure 1. This technique has three time delays, as in 2D IR spectroscopy.[11] Since the IIIV signal is in the visible region, its detection is easier than the second-order IR−IR signal.

Here we examine the spectral diffusion of interfacial water near DMPC by a simulation study of the IIIV signal. This is the first reported simulation of the fourth-order IIIV signal. The marriage of the homodyne-detected fourth-order spectroscopy technique[10] with heterodyne-detected SFG[12] should make the proposed heterodyne-detected fourth-order spectroscopy possible in the near future. Our simulation protocol is fully classical and involves two steps. First, classical MD simulations are used to compute the fluctuating

Received: November 30, 2010
Published: February 18, 2011

dx.doi.org/10.1021/ja110748s | *J. Am. Chem. Soc.* 2011, 133, 3276–3279

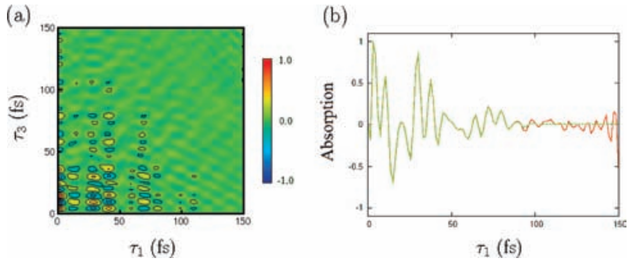

Figure 2. (a) Time-domain 2D response function $R^{(4)}_{xxzzz}(\tau_3, \tau_2 = 0, \tau_1)$. (b) Diagonal elements of time-domain 2D response functions. Red and green lines represent the bare response function $R^{(4)}_{xxzzz}(\tau_1, \tau_2 = 0, \tau_1)$ and smoothed response function $R^{(4)}_{s,xxzzz}(\tau_1, \tau_2 = 0, \tau_1)$, respectively.

ensemble of structural configurations. Second, the nonlinear response is treated as classical using the same force field. Quantum simulations of response function, on the other hand, commonly use the same classical first step, but for the second step they require the construction of an effective Hamiltonian for the optically active vibrations, which is different from the field used in the first step.[11] This Hamiltonian must be parameterized vs. molecular geometry and electrostatic interactions with other degrees of freedom. This is not required in the classical protocol which can use the same Hamiltonian and classical trajectories for both steps. Note, however, that in the present simulations we used the non-polarizable force field for step one and the induced effect is only included in step two. Because of the complicated parameterization, the quantum simulations typically use a few vibrational modes which must be selected beforehand, whereas including all vibrational modes as well as relaxations and dephasing process is straightforward in the classical simulations. Classical simulations also avoid diagonalizations of the Hamiltonian which is required in quantum simulations. The present classical protocol is suitable for complex highly disordered systems. Our main findings are an asymmetric cross-peak pattern in the 2D spectra representing coherence transfer; a steep nodal slope for the H mode, indicating slow spectral diffusion of top-layer water; and a shallow nodal slope for the L mode, indicating fast spectral diffusion of near-bulk water. The gradient of the nodal slope of the L mode indicates that the spectral diffusion of near-bulk water is as fast as that of bulk water, even though the near-bulk water is oriented to DMPC, unlike bulk water.

A system consists of eight DMPC and 462 water molecules. Details of the MD simulation protocols are given in the Supporting Information. The classical approximation holds when the vibrational frequency is low relative to k_BT, where T is the system temperature, or for weakly anharmonic vibrations at any temperature. The OH stretch is weakly anharmonic (the vibrational frequency is ~3700 cm^{-1} and the frequency shift due to the anharmonic potential is ~150 cm^{-1}), which makes the classical protocol adequate for the present application. The merits of this approach are given in the Supporting Information. The fourth-order IIIV response function was calculated classically using the stability matrix formalism:[13,14]

$$R^{(4)}_{abcde}(\tau_3, \tau_2, \tau_1) = -\beta\langle\{A_{ab}(t_3), M_c(t_2)\}(\beta \dot{M}_d(t_1)\dot{M}_e(t_0) - \{M_d(t_1), \dot{M}_e(t_0)\})\rangle \qquad (1)$$

where $\beta = 1/k_BT$; $T = 300$ K; $t_3 = \tau_3 + \tau_2/2$, $t_2 = \tau_2/2$, $t_1 = -\tau_2/2$, and $t_0 = -\tau_1 - \tau_2/2$; a, b, c, d, e represent the pulse polarization directions; τ_1, τ_2, and τ_3 are the delays between pulses (Figure 1); $M(t)$ and $A(t)$ are the total dipole moment and total polarizability of the entire system at time t, respectively; and $\{\cdots\}$ denotes the Poisson bracket. Calculation details for $M(t)$ and $A(t)$ are given in the Supporting Information.

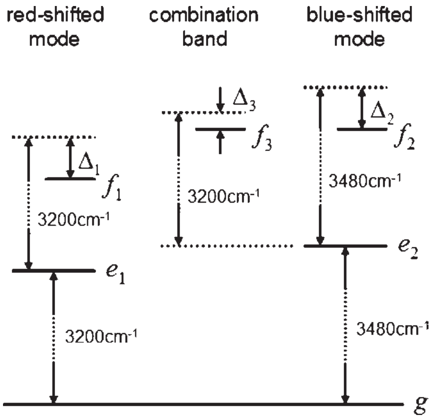

Figure 3. Energy-level scheme for the water OH stretch at the DMPC interface. The symbols g, e_j $(j = 1, 2)$, and f_k $(k = 1-3)$ represent the ground, one-exciton, and two-exciton states. Δ_1, Δ_2, and Δ_3 denote the frequency shifts of the two-exciton states.

In all of the simulations, we set the waiting time (τ_2) to zero. Variation of the signal with τ_2 should directly reveal vibrational relaxation. This goes beyond the present study. The time-domain fourth-order response function, $R^{(4)}_{xxzzz}(\tau_3, \tau_2 = 0, \tau_1)$, is displayed in Figure 2a. The signal decays in ~80 fs along the τ_3 axis. To suppress the small fluctuations at long τ_3 and τ_1, we employed the window function[9,14]

$$f_s(\tau_s) = \begin{cases} 1 & \text{for} \quad \tau_s < t_{c1} \\ \cos^2[\pi(\tau_s - t_{c1})/2(t_{c2} - t_{c1})] & \text{for} \quad t_{c1} \le \tau_s < t_{c2} \\ 0 & \text{for} \quad t_{c2} \le \tau_s \end{cases} \qquad (2)$$

where $\tau_s = (\tau_1^2 + \tau_3^2)^{1/2}$, $t_{c1} = 112.5$ fs, and $t_{c2} = 150$ fs, and defined the smoothed response function $R^{(4)}_{s,xxzzz}(\tau_3, \tau_2 = 0, \tau_1) = R^{(4)}_{xxzzz}(\tau_3, \tau_2 = 0, \tau_1) f_s(\tau_s)$. The diagonal element of the smoothed response function $R^{(4)}_{s,xxzzz}(\tau_1, \tau_2 = 0, \tau_1)$ is compared with that of the bare response function $R^{(4)}_{xxzzz}(\tau_1, \tau_2 = 0, \tau_1)$ in Figure 2b.

The frequency-domain 2D spectra were obtained by a double Fourier transform of the time-domain response function:

$$R^{(4)}_{abcde}(\omega_3, \tau_2 = 0, \omega_1) = \int_0^\infty d\tau_1 \int_0^\infty d\tau_3 \, e^{-i\omega_1\tau_1 - i\omega_3\tau_3} R^{(4)}_{s,abcde}(\tau_3, \tau_2 = 0, \tau_1) \qquad (3)$$

$R^{(4)}_{xxzzz}(\omega_3, \tau_2, \omega_1)$ includes all possible Liouville space pathways that contribute to different signals. Denoting the wavevectors of the IR pulses by $\mathbf{k}_1$, $\mathbf{k}_2$, and $\mathbf{k}_3$ and that of the visible pulse by $\mathbf{k}_4$, we have the rephasing signal at $\mathbf{k}_\mathrm{I} = -\mathbf{k}_1 + \mathbf{k}_2 + \mathbf{k}_3 + \mathbf{k}_4$, the nonrephasing signal at $\mathbf{k}_\mathrm{II} = \mathbf{k}_1 - \mathbf{k}_2 + \mathbf{k}_3 + \mathbf{k}_4$, and the double-quantum coherence signal at $\mathbf{k}_\mathrm{III} = \mathbf{k}_1 + \mathbf{k}_2 - \mathbf{k}_3 + \mathbf{k}_4$. In this study, we focus on the $\mathbf{k}_\mathrm{I}$ signal, which appears in the region for which $\omega_1 < 0$ and $\omega_3 > 0$. The $\mathbf{k}_\mathrm{II}$ and $\mathbf{k}_\mathrm{III}$ signals are easily separated, since they appear in the region for which $\omega_1 > 0$ and $\omega_3 > 0$.

Our model includes all vibrational modes of water, which are treated classically. The effective vibrational energy level scheme obtained from the simulated 1D SFG spectrum for the OH stretch at the DMPC interface is presented in Figure 3. Here $|g\rangle$

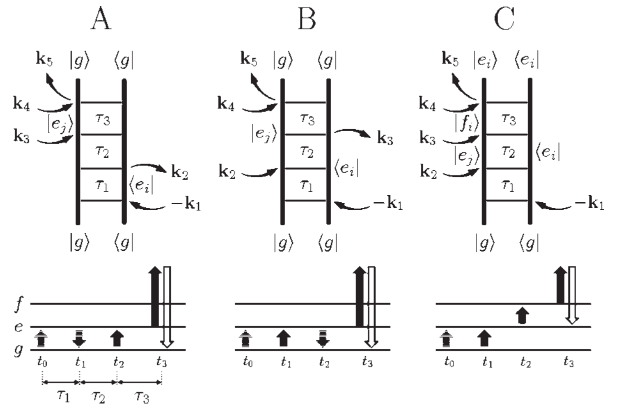

Figure 4. Top panels: Feynman diagrams for the fourth-order IIIV signal at $\mathbf{k}_I = -\mathbf{k}_1 + \mathbf{k}_2 + \mathbf{k}_3 + \mathbf{k}_4$. Bottom panels: energy level scheme. The transitions of the bra and ket are denoted as solid and shadowed arrows, respectively, and the detection pulses are denoted by the open arrows.

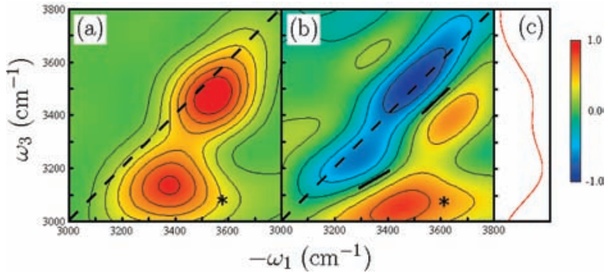

Figure 5. (a, b) Simulated fourth-order spectra in the direction $\mathbf{k}_I = -\mathbf{k}_1 + \mathbf{k}_2 + \mathbf{k}_3 + \mathbf{k}_4$: (a) $|R^{(4)}_{xxzzz}(\omega_3, \tau_2 = 0, \omega_1)|^2$; (b) $\mathrm{Im}[R^{(4)}_{xxzzz}(\omega_3, \tau_2 = 0, \omega_1)]$. The cross-peaks are marked by asterisks (*). The black solid lines in (b) represent the nodal lines between negative and positive peaks. The angles between the nodal lines and the $-\omega_1$ axis are 29° for the L mode and 44° for the H mode. The frequencies of the L and H modes are 3480 and 3200 cm^{-1}, respectively. (c) SFG spectrum $\mathrm{Im}[R^{(2)}_{xxz}(\omega_3)]$.

represents the ground state; the singly excited L and H states are denoted as $|e_1\rangle$ and $|e_2\rangle$, respectively, while the doubly excited states of the L and H modes and the combination state are denoted as $|f_1\rangle$, $|f_2\rangle$, and $|f_3\rangle$, respectively. The three Liouville space pathways contributing to the $\mathbf{k}_I$ signal are shown in Figure 4. Peaks in $\mathrm{Im}[R^{(4)}_{xxzzz}(\omega_3, \tau_2, \omega_1)]$ corresponding to diagrams A and B have signs opposite those for diagram C. When the frequency shifts of doubly excited states or the combination state are zero, these opposite-sign contributions exactly cancel, as in 2D IR spectra. The information on the molecular orientation contained in $\mathrm{Im}[R^{(2)}_{xxz}(\omega)]$ also shows up in $\mathrm{Im}[R^{(4)}_{xxzzz}(\omega_3, \tau_2 = 0, \omega_1)]$: peaks corresponding to diagrams A and B in $\mathrm{Im}[R^{(4)}_{xxzzz}(\omega_3, \tau_2 = 0, \omega_1)]$ have signs opposite those in $\mathrm{Im}[R^{(2)}_{xxz}(\omega)]$.

The frequency-domain 2D spectra, $|R^{(4)}_{xxzzz}(\omega_3, \tau_2 = 0, \omega_1)|^2$ and $\mathrm{Im}[R^{(4)}_{xxzzz}(\omega_3, \tau_2 = 0, \omega_1)]$, are displayed in Figure 5a,b, respectively. In Figure 5a, the H peak is on the diagonal line $-\omega_1 = \omega_3$, whereas the L peak appears in the $-\omega_1 > \omega_3$ region. Both signals show weak cross-peaks in the $-\omega_1 > \omega_3$ region (marked by asterisks) but no cross-peaks in the $-\omega_1 < \omega_3$ region.

The diagonal peaks in Figure 5b show that the frequency shifts were $\Delta_1 = 180$ cm^{-1} for the L mode and $\Delta_2 = 150$ cm^{-1} for the H mode. These are close to the frequency shift of 153 cm^{-1} due to the intramolecular anharmonicity of the water OH stretch.[15] The peaks overlap, since Δ_1 and Δ_2 are comparable with the frequency splitting of $\Delta\omega = 280$ cm^{-1} for the L and H peaks. In particular, the positive peak of the H mode and the negative peak of the L mode cancel out because the latter peak is elongated along the ω_1 axis, as schematically illustrated in Figure 6. This cancellation weakens the negative peak of the L mode and shifts the peak in $|R^{(4)}_{xxzzz}(\omega_3, \tau_2 = 0, \omega_1)|^2$ to the $-\omega_1 > \omega_3$ region.

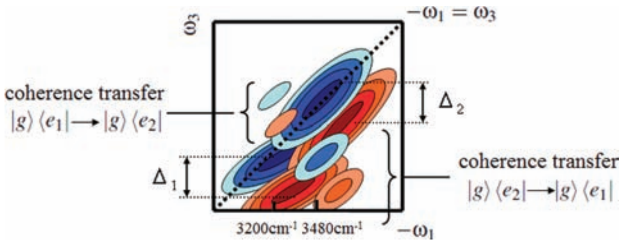

Figure 6. Schematic 2D spectrum for $\mathrm{Im}[R^{(4)}_{xxzzz}(\omega_3, \tau_2 = 0, \omega_1)]$ that helped in the peak assignment. Coherence transfer from $|g\rangle\langle e_2|$ to $|g\rangle\langle e_1|$ is responsible for the triangular cross-peak in the $-\omega_1 > \omega_3$ region, while coherence transfer from $|g\rangle\langle e_1|$ to $|g\rangle\langle e_2|$ causes the cross-peak in the $-\omega_1 < \omega_3$ region.

We next turn to the cross-peaks, for which there are two possible origins. One is the frequency shift for the combination band of the L and H modes. If the L and H modes are coupled and this lowers the frequency of the combination mode by Δ_3, the cross-peaks appear in both the $-\omega_1 > \omega_3$ and $-\omega_1 < \omega_3$ regions with equal intensities. The absence of a cross-peak in the $-\omega_1 < \omega_3$ region means that the direct intermode coupling is weak in comparison with the intramolecular anharmonicity, and $\Delta_3 \ll \Delta_1 \approx \Delta_2$. Cross-peaks can also originate from coherence transfer from $|g\rangle\langle e_2|$ to $|g\rangle\langle e_1|$ and from $|g\rangle\langle e_1|$ to $|g\rangle\langle e_2|$ during τ_1 and τ_3 using detailed balance. The $\Delta\omega = 280$ cm^{-1} energy splitting of the L and H modes indicates that the transition from $|g\rangle\langle e_2|$ to $|g\rangle\langle e_1|$ is $\exp(\Delta\omega/k_BT) \approx 3.8$ times faster than the transition from $|g\rangle\langle e_1|$ to $|g\rangle\langle e_2|$. Coherence transfer from $|g\rangle\langle e_2|$ to $|g\rangle\langle e_1|$ creates the cross-peak in the $-\omega_1 > \omega_3$ region, while the cross peak in the $-\omega_1 < \omega_3$ region arises from coherence transfer from $|g\rangle\langle e_1|$ to $|g\rangle\langle e_2|$. Thus, $\mathrm{Im}[R^{(4)}_{xxzzz}(\omega_3, \tau_2 = 0, \omega_1)]$ show a cross-peak in the $-\omega_1 > \omega_3$ region, while the cross-peak in the $-\omega_1 < \omega_3$ region is weak and not clearly observed, as illustrated in Figure 6.

Spectral diffusion of water at the DMPC interface can be inferred from the angle between the nodal lines and the $-\omega_1$ axis in Figure 5b; the nodal line parallel to the diagonal indicates slow spectral diffusion in comparison with the decay time of the signal of ~80 fs, while the nodal line parallel to the ω_1 axis indicates fast spectral diffusion.[16] In Figure 5, the angles are 29° for the L mode and 44° for the H mode. Since the H mode was assigned to the top-layer OH stretch adjacent to DMPC,[4] we conclude that this OH stretch has slow spectral diffusion because of the strong electrostatic interactions between water and the hydrophilic part of DMPC. The heterogeneous nature of water at DMPC with low hydration was also reported by Volkov et al..[5] Figure 5b also shows that the L mode has a shallow nodal slope in comparison with the H mode, indicating that the near-bulk OH stretch nonadjacent to DMPC has faster spectral diffusion than the OH stretch adjacent to DMPC. The angle of 29° in $\mathrm{Im}[R^{(4)}_{xxzzz}(\omega_3, \tau_2 = 0, \omega_1)]$ is remarkably close to 30 ± 5° found in the 2D IR spectrum of bulk water.[17] This means that the interfacial water corresponding to the L mode changes the frequency of its OH stretch rapidly as a result of the ultrafast conformational changes at a speed similar to that for bulk water. Unlike bulk water, the near-bulk water nonadjacent to DMPC is oriented to DMPC. Nevertheless, the water dynamics is similar in these two cases.

In conclusion, we have reported the first simulation study of the 2D fourth-order IIIV rephasing signal, $\mathbf{k}_\mathrm{I} = -\mathbf{k}_1 + \mathbf{k}_2 + \mathbf{k}_3 + \mathbf{k}_4$, at the water/DMPC interface. Both of the simulated signals, $|R^{(4)}_{xxzzz}(\omega_3, \tau_2 = 0, \omega_1)|^2$ and $\mathrm{Im}[R^{(4)}_{xxzzz}(\omega_3, \tau_2 = 0, \omega_1)]$, show a cross-peak in the $-\omega_1 > \omega_3$ region and no cross-peaks in the $-\omega_1 < \omega_3$ region, indicating coherence transfer from the H mode to the L mode. $\mathrm{Im}[R^{(4)}_{xxzzz}(\omega_3, \tau_2 = 0, \omega_1)]$ shows that the L mode has a shallower nodal slope than the H mode, and the gradient of the nodal line for the L mode is similar to that for bulk water in 2D IR spectra. These results indicate that the H and L modes have fast and slow spectral diffusion, respectively. By using the peak assignments of the H and L modes in our previous work,[4] we can conclude that the near-bulk water nonadjacent to DMPC has faster spectral diffusion than the top-layer water adjacent to DMPC and that its spectral diffusion time scale is similar to that of bulk water.

■ ASSOCIATED CONTENT

Ⓢ **Supporting Information.** Derivation of the classical response function for the fourth-order signal, protocols for the MD simulation and the calculation of the optical response, and simulated SFG spectra. This material is available free of charge via the Internet at http://pubs.acs.org.

■ AUTHOR INFORMATION

Corresponding Author

nagatay@uci.edu

■ ACKNOWLEDGMENT

This work was supported by the National Institute of Health (Grant GM-59230) and the National Science Foundation (Grant CHE-0745892).

■ REFERENCES

(1) Egberts, E.; Marrink, S. J.; Berendsen, H. J. C. *Eur. Biophys. J.* **1994**, *22*, 423–436.

(2) (a) Mondal, J. A.; Nihonyanagi, S.; Yamaguchi, S.; Tahara, T. *J. Am. Chem. Soc.* **2010**, *132*, 10656. (b) Chen, X. K.; Hua, W.; Huang, Z. S.; Allen, H. C. *J. Am. Chem. Soc.* **2010**, *132*, 11336–11342.

(3) (a) Ghosh, A.; Smits, M.; Bredenbeck, J.; Bonn, M. *J. Am. Chem. Soc.* **2007**, *129*, 9608. (b) Ghosh, A.; Smits, M.; Sovago, M.; Bredenbeck, J.; Bonn, M. *Chem. Phys. Lett.* **2008**, *350*, 23–30.

(4) Nagata, Y.; Mukamel, S. *J. Am. Chem. Soc.* **2010**, *132*, 6434–6442.

(5) (a) Volkov, V. V.; Palmer, D. J.; Righini, R. *J. Phys. Chem. B* **2007**, *111*, 1377–1382. (b) Volkov, V. V.; Palmer, D. J.; Righini, R. *Phys. Rev. Lett.* **2007**, *99*, No. 078302. (c) Volkov, V. V.; Kataoka, Y.; Righini, R. *J. Phys. Chem. B* **2009**, *113*, 4119–4124.

(6) Szyc, L.; Yang, M.; Nibbering, E. T. J.; Elsaesser, T. *Angew. Chem., Int. Ed.* **2010**, *49*, 3598–3610.

(7) Tanimura, Y.; Mukamel, S. *J. Chem. Phys.* **1993**, *99*, 9496–9511.

(8) Cho, M. *J. Chem. Phys.* **2000**, *112*, 9978–9985.

(9) Nagata, Y.; Tanimura, Y.; Mukamel, S. *J. Chem. Phys.* **2007**, *126*, No. 204703.

(10) (a) Bredenbeck, J.; Ghosh, A.; Smits, M.; Bonn, M. *J. Am. Chem. Soc.* **2008**, *130*, 2152–2153. (b) Bredenbeck, J.; Ghosh, A.; Nienhuys, H. K.; Bonn, M. *Acc. Chem. Res.* **2010**, *42*, 1332–1342.

(11) Mukamel, S.; Abramavicious, D. *Chem. Rev.* **2004**, *104*, 2073–2098.

(12) (a) Stiopkin, I. V.; Jayathilake, H. D.; Bordenyuk, A. N.; Benderskii, A. V. *J. Am. Chem. Soc.* **2008**, *130*, 2271–2275. (b) Nihonyanagi, S; Yamaguchi, S.; Tahara, T. *J. Chem. Phys.* **2009**, *130*, No. 204704.

(13) (a) Mukamel, S.; Khidekel, V.; Chernyak, V. *Phys. Rev. E* **1996**, *53*, R1–R4. (b) Saito, S.; Ohmine, I. *J. Chem. Phys.* **1998**, *108*, 240–251.

(14) Jeon, J.; Cho, M. *New J. Phys.* **2010**, *12*, No. 065001.

(15) Hayashi, T.; Jansen, T. l. C.; Zhuang, W.; Mukamel, S. *J. Phys. Chem. A* **2005**, *109*, 64–82.

(16) Roberts, S. T.; Ramasesha, K.; Tokmakoff, A. *Acc. Chem. Res.* **2009**, *42*, 1239–1249.

(17) (a) Asbury, J. B.; Steinel, T.; Stromberg, C.; Corcelli, S. A.; Lawrence, C. P.; Skinner, J. L.; Fayer, M. D. *J. Phys. Chem. A* **2004**, *108*, 1107–1119. (b) Eaves, J. D.; Loparo, J. J.; Fecko, C. J.; Roberts, S. T.; Tokmakoff, A.; Geissler, P. L. *Proc. Natl. Acad. Sci. U.S.A.* **2005**, *102*, 13019–13022. (c) Jansen, T. l. C.; Auer, B. M.; Yang, M.; Skinner, J. L. *J. Chem. Phys.* **2010**, *132*, No. 224503.